CHEMISTRY OF MATERIALS

pubs.acs.org/cm

Article

Constructing Synergistic Triazine and Acetylene Cores in Fully Conjugated Covalent Organic Frameworks for Cascade Photocatalytic H_2O_2 Production

Lipeng Zhai,[#] Zhipeng Xie,[#] Cheng-Xing Cui,[#] Xiubei Yang, Qing Xu,* Xiating Ke, Minghao Liu, Ling-Bo Qu, Xiong Chen,* and Liwei Mi*

Cite This: https://doi.org/10.1021/acs.chemmater.2c00910

Read Online

ACCESS | Metrics & More | Article Recommendations | Supporting Information

ABSTRACT: Covalent organic frameworks (COFs) are an ideal template for photocatalytic H_2O_2 synthesis because of the tunable chemical structures and semiconductor properties. However, the photoactivity for COFs is still under-improved due to the inefficient intrinsic charge generation, fast recombination of photogenerated charges, and limited electron transport along the frameworks. Herein, spatially separated and synergistic triazine and acetylene units are first integrated into COFs (EBA-COF and BTEA-COF) for photocatalytic H_2O_2 production. The spatial separation of triazine and acetylene cores leads to efficient charge separation and suppressed charge recombination, and C═C linkage facilitates electrons transport over the skeletons. Both experimental and computational results suggested that triazine and acetylene units synergistically promote H_2O_2 synthesis in a two-electron pathway. The EBA-COF showed an attractive activity with a H_2O_2 production rate of 1830 μmol h^{-1} g_{cat}^{-1}, superior to that of most other COF-based catalysts. This study provides a method for designing photocatalysts with synergistic photocatalytic active sites based on vinylene-linked COFs.

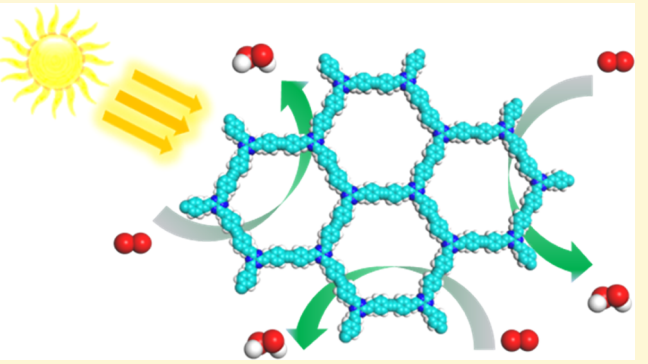

INTRODUCTION

Hydrogen peroxide (H_2O_2) is recognized as a multifunctional and essential chemical owing to its strong oxidative and bleaching abilities and is widely utilized in semiconductor manufacturing, wastewater treatment, bleaching, and chemical synthesis.[1−5] Moreover, H_2O_2 is regarded as a powerful potential energy carrier since it can be employed directly in fuel cells for electricity production.[6−9] Currently, the industrial production of H_2O_2 is primarily dependent on the energy-intensive anthraquinone process, which includes the hydrogenation reaction over Pd, oxidation, and multistep solvent extraction.[10−16] Although the direct synthesis of H_2O_2 from H_2 and O_2 using metal catalysts (Pd or Au−Pd catalysts) is feasible, this method is considered unsafe due to its use of mixed H_2/O_2 and its potentially explosive nature.

Unlike anthraquinone oxidation and direct synthesis methods, photocatalytic H_2O_2 generation from H_2O and O_2 can be achieved by reducing the dissolved oxygen via photogenerated electrons over semiconductors, in a technology that is considered as promising, economical, and eco-friendly.[17−21] To date, considerable efforts have been devoted to the rational design and synthesis of efficient photocatalysts such as TiO_2, polymeric carbon nitride, metal−organic compounds, triazine-based frameworks (CTFs), and linear polymers. The enhanced photon capture and facilitated charge separation capabilities were constructed to achieve highly efficient solar-driven H_2O_2 conversion.[22−25] Recent studies have indicated that metal-free polymer photocatalysts provide a powerful platform for photocatalytic H_2O_2 production. Compared to inorganic photocatalysts, metal-free polymer photocatalysts generally exhibit much higher activity and selectivity toward H_2O_2 production by forming suitable intermediates and eliminating side reactions.[26−28] Although promising and exciting results have been made, designing materials for efficient photocatalytic production of H_2O_2 is still in the beginning stage, and further development is strongly required for future practical applications. In addition, the reported photocatalysts still are facing the challenge of low yield of H_2O_2, which is much lower than that required by industrially practical applications.

Owing to their structural regularity, designable topology, and functionality, covalent organic frameworks (COFs) with

Received: March 24, 2022
Revised: May 4, 2022

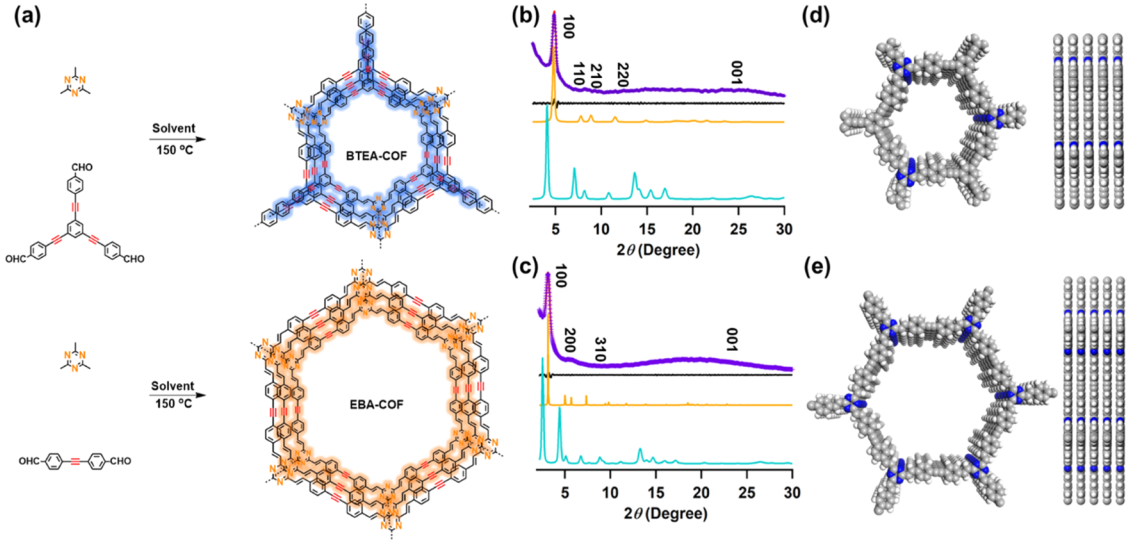

Figure 1. (a) Scheme of the synthetic process of BTEA-COF and EBA-COF. Powder X-ray diffraction (PXRD) patterns for BTEA-COF (b) and EBA-COF (c): experimental (red) and Pawley refined (purple) PXRD profiles, the corresponding difference (black), and the simulated curves for the eclipsed AA stacking mode (orange) and AB stacking mode (cyan). Top view and side view of the AA packing model of BTEA-COF (d) and EBA-COF (e).

crystalline 2D ordered structures have emerged as a promising material design platform for photocatalysts.[29−39] However, using COFs as photocatalysts for H_2O_2 production is still rare. In 2020, Voort et al. reported two COFs based on a (diarylamino) benzene linker for photocatalytic H_2O_2 production for the first time.[40] Subsequently, Yu et al. attempted to optimize the H_2O_2 evolution rates via a gas−liquid−solid interface.[41] In 2022, Ma et al. reported several COFs for photocatalytic H_2O_2 production via molecular engineering.[42] However, to the best of our knowledge, these are no reported vinylene-linked COFs for photocatalytic H_2O_2 production, where the photocatalytic activity of COFs can be further enhanced owing to the efficient intrinsic charge generation, suppressed recombination of photogenerated charges, and strong electron transport ability in the skeletons of this kind COFs. Therefore, the development of COFs with excellent photocatalytic H_2O_2 production activity has yet to be achieved and requires new molecular designs and synthetic strategies.

Recently, vinylene-linked COFs have received increasing attention owing to their extended π-conjugation, excellent charge carrier mobility, and ultrahigh chemical stability even under harsh conditions.[43−53] These unique features enable the use of vinylene-linked COFs as photocatalysts for H_2O_2 production. Recently, Xu et al. reported the first case of the spatial separation of reduction and oxidation centers in a single polymer photocatalyst for efficient H_2O_2 production using *s*-heptazine and acetylene moieties or diacetylene bonds.[54] This unique spatial separation feature provided significantly reduced exciton binding energy, enhanced charge transfer ability, and suppressed charge recombination, which are essential for efficient charge separation and lead to superior photocatalytic activity. Nevertheless, to the best of our knowledge, the construction of vinylene-linked COFs with spatially separated photocatalytic reactive centers has not been explored. In this study, we synthesized two vinylene-linked COFs with a triazine unit and different acetylene-containing building linkers via Knoevenagel polymerization. Thus, spatially separated photocatalytic reactive centers were realized, and enhanced photocatalytic H_2O_2 generation was achieved for the first time with this type of COFs. Furthermore, the electron-deficient triazine moiety exhibited high electron affinity owing to the high content of nitrogen atoms, and acetylenic groups act as a bridge between electron donors and acceptors to achieve the efficient transfer of photogenerated electrons.

EXPERIMENTAL SECTION

Synthesis of the EBA-COF. A Pyrex tube (10 mL) was charged with 2,4,6-trimethyl-1,3,5-triazine (TM, 12.32 mg, 0.1 mmol), 4,4′-(ethyne-1,2-diyl) dibenzaldehyde (EBA, 35.14 mg, 0.15 mmol), 0.9 mL of mesitylene, 0.9 mL of 1,4-dioxane, 0.40 mL of trifluoroacetic acid, and 50 μL of acetonitrile. The tube was then flash-frozen at 77 K and degassed by three freeze−pump−thaw cycles. The tube was sealed and heated at 150 °C for 3 days. The collected powder was neutralized using 0.1 mol L^{-1} NH_4OH solution in aqueous methanol (50 wt %) and washed with tetrahydrofuran (THF) and methanol. The solid was then washed with methanol in a Soxhlet extractor for another 12 h. Subsequently, the product was dried at 120 °C under vacuum for 12 h to obtain the corresponding yellow powder in ∼85% isolated yield.

Synthesis of the BTEA-COF. A Pyrex tube (10 mL) was charged with 2,4,6-trimethyl-1,3,5-triazine (TM, 12.3 mg, 0.1 mmol), 4,4′,4″-(benzene-1,3,5-triyltris(ethyne-2,1-diyl)) tribenzaldehyde (BTEA, 46.25 mg, 0.1 mmol), 0.9 mL of mesitylene, 0.9 mL of 1,4-dioxane, 0.40 mL of trifluoroacetic acid, and 50 μL of acetonitrile. The tube was then flash-frozen at 77 K and degassed by three freeze−pump−thaw cycles. The tube was sealed and heated at 150 °C for 3 days. The collected powder was neutralized with 0.1 mol L^{-1} NH_4OH solution in aqueous methanol (50 wt%) and washed with THF and methanol. The solid was then washed with methanol in a Soxhlet extractor for another 12 h. The product was then dried at 120 °C under vacuum for 12 h to obtain the corresponding yellow powder in ∼87% isolated yield.

DISCUSSION

In this study, two vinylene-linked COFs (EBA-COF and BTEA-COF) were synthesized from the electron-deficient monomer 2,4,6-trimethyl-1,3,5-triazine and electron-rich monomers 4,4′-(ethyne-1,2-diyl) dibenzaldehyde (EBA) or 4,4′,4″-(benzene-1,3,5-triyltris(ethyne-2,1-diyl)) tribenzalde-

https://doi.org/10.1021/acs.chemmater.2c00910
Chem. Mater. XXXX, XXX, XXX−XXX

hyde (BTEA) in a solvent mixture of 1,4-dioxane, mesitylene, and acetonitrile using trifluoroacetic acid as the catalyst at 150 °C for 72 h in 85 and 87% yields, respectively (Figure 1a). The detailed chemical structures of both COFs were then studied using various measurements. As shown in Fourier transform infrared (FT-IR) spectroscopy (Figure S1), unlike the aldehyde monomers, the disappearance of the C═O stretching bands for the two synthesized COFs (1692 cm^{-1}) indicated a high degree of polymerization. In addition, the new peaks at 1631 and 985 cm^{-1} in the FT-IR spectra were attributed to the C═C stretching and C═C trans-configurations, respectively, which indicated the formation of C═C bonds for both COFs. The peak at 2193 cm^{-1} was assigned to the C≡C units for both COFs. Their chemical structures were further confirmed by ^{13}C cross-polarization/magic-angle spinning solid-state nuclear magnetic resonance (^{13}C CP/MAS-ssNMR, Figures S2 and S3). The peaks around 171, 138, and 89 ppm in the ^{13}C CP/MAS-ssNMR spectra were assigned to the carbon in the triazine units, C≡C, and C═C bonds, respectively, for both COFs. The elemental analysis of both COFs indicated that the contents of C, H, and N were close to the theoretical values based on the infinite 2D sheet (Table S1). Thermogravimetric analysis (TGA) showed that both COFs exhibited no distinct decomposition before 400 °C under N_2 (Figure S4). Comparably, both COFs are stable up to 170 °C under an air atmosphere (Figure S5). Field emission scanning electron microscopy (FE-SEM) was used to study the morphology of the two COFs. As shown in Figure S6, both COFs exhibited uniform spherical morphologies. In addition, the elements of these two COFs were distributed uniformly over the networks (Figures S7 and S8) based on EDX mapping results.

The crystallinities of the as-prepared COFs were assessed using powder X-ray diffraction (PXRD) measurements. EBA-COF exhibited four distinct diffraction peaks, with the most intense peak at 3.2° and three other peaks at 5.70, 9.80, and 25.64°, which were attributed to the 100, 200, 310, and 001 facets, respectively (Figure 1b, red curve). The PXRD patterns of the BTEA-COF showed diffraction peaks at 4.78, 7.76, 11.52, 14.76, and 25.78°, which were assigned to the 100, 110, 210, 220, and 001 facets, respectively (Figure 1c, red curve). Pawley refinements were applied to investigate the theoretical structures with the self-consistent charge density functional tight binding (SCC-DFTB) method. As shown in Figure 1b,c, good agreement and negligible residue values were found for the EBA-COF (5.93% for R_{wp} and 4.69% for R_p) and BTEA-COF (6.11% for R_{wp} and 5.06% for R_p), respectively. As for the stacking mode of these two COFs, eclipsed AA packing afforded a better match with the intensities of the peaks in the experimental PXRD pattern, as evidenced by the negligible difference (Figure 1b,c, black curves), where Pawley refinements were applied to rebuild cell parameters using the hexagonal space group: $a = b = 34.3767$ Å, $c = 3.5355$ Å, $\alpha = \beta = 90°$, and $\gamma = 120°$ for the EBA-COF and $a = b = 23.1146$ Å, $c = 3.5350$ Å, $\alpha = \beta = 90°$, and $\gamma = 120°$ for the BTEA-COF. The corresponding top view and side view of the AA packing model of the BTEA-COF (Figure 1d) and EBA-COF (Figure 1e) are shown.

The prominent porosities of the EBA-COF and BTEA-COF were investigated by nitrogen physisorption measurements at 77 K. As shown in Figure 2a, the EBA-COF displays a typical I isotherm, which is indicative of a microporous structure. The BTEA-COF shows a typical IV isotherm with mesoporous

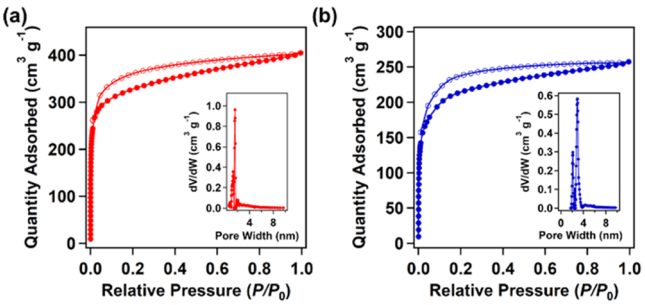

Figure 2. Nitrogen sorption isotherms measured at 77 K: (a) BTEA-COF and (b) EBA-COF. Inset: pore size distribution profiles.

characteristics (Figure 2b). The Brunauer−Emmett−Teller (BET) surface areas for the EBA-COF and BTEA-COF were calculated to be 740 and 1113 m^2 g^{-1}, respectively. The pore size distribution profiles obtained using the NLDFT model revealed that the pore sizes for the EBA-COF and BTEA-COF were 1.9 and 3.1 nm, respectively. Moreover, the pore sizes of these two COFs were in line with their AA-eclipsed modes. The corresponding pore volumes for the EBA-COF and BTEA-COF were 0.59 and 0.97 cm^3 g^{-1}, respectively.

The chemical stabilities of the BTEA-COF and EBA-COF toward water (H_2O), ethanol, HCl (1 M), and NaOH (1 M) were characterized, and the related PXRD and FT-IR curve comparison before and after the chemical stability test was added in the Supporting Information. As shown in Figures S9 and S10, both COFs had similar PXRD patterns and FT-IR curves after treatment in different solvents at room temperature after 3 days, indicating that both COFs could retain their original structures and displayed excellent stability.

The optoelectronic properties were investigated by ultraviolet/visible absorption diffuse reflectance spectroscopy (UV−vis DRS) and fluorescence spectroscopy. In the UV−vis DRS analysis, the EBA-COF and BTEA-COF exhibited strong absorptions around 618 and 595 nm, respectively (Figure 3a). The corresponding Tauc plot analysis from the UV−vis DRS exhibited optical energy band gaps of 2.39 and 2.41 eV for the EBA-COF and BTEA-COF, respectively (Figure S11), indicating that both COFs are suitable for absorbing visible light for photocatalysis. Mott−Schottky (M−S) measurements were conducted to study the electronic structure and relative band positions of these two COFs. The positive slope indicated typical n-type semiconductor characteristics for the EBA-COF and BTEA-COF, and the corresponding flat-band potentials (E_{fb}) of the EBA-COF and BTEA-COF were fitted to be −0.72 and −0.60 V vs the normal hydrogen electrode (NHE) at pH 7 from the intercept of the linear region of the M−S plots, respectively (Figure 3b,c). Combining the Tauc plot and M−S plot, the corresponding band positions of the EBA-COF and BTEA-COF were calculated. The valence band maximum (E_{VBM}) values for the EBA-COF and BTEA-COF were evaluated to be 1.89 and 1.99 eV, respectively. The conduction band minimum (E_{CBM}) values were calculated to be −0.52 and −0.4 eV for the EBA-COF and BTEA-COF, respectively (Figure 3d). The lower E_{CBM} of the EBA-COF compared with that of the BTEA-COF indicates that the EBA-COF is likely to exhibit better electron transport capacity during the photocatalytic process. Furthermore, the energy level for the reduction of O_2 to O_2^- was observed to be below E_{CBM}, while that for the oxidation of H_2O to H_2O_2 was above the E_{VBM} of both COFs. The band

https://doi.org/10.1021/acs.chemmater.2c00910
Chem. Mater. XXXX, XXX, XXX−XXX

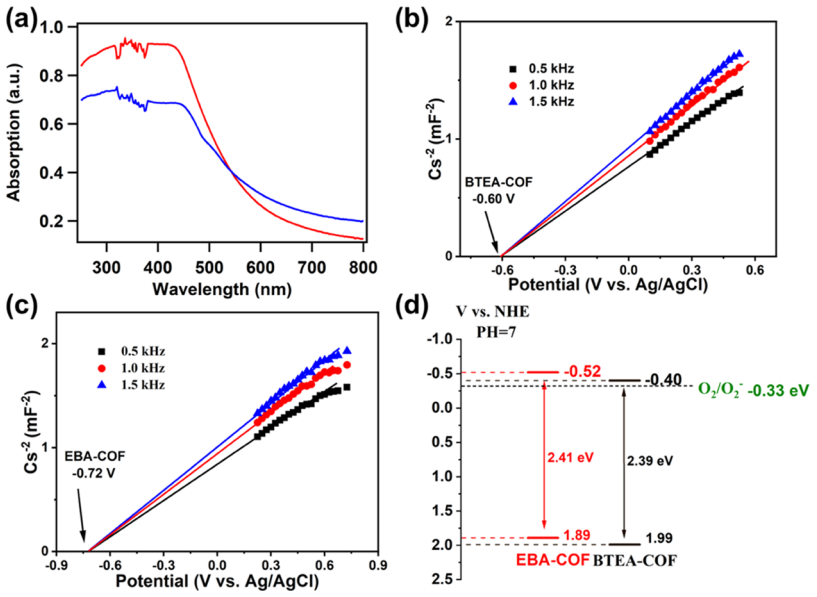

Figure 3. (a) UV-DRS of the BTEA-COF (red) and EBA-COF (blue). Mott−Schottky plot of the BTEA-COF (b) and EBA-COF (c) showing the flat-band potential using the conventional three-electrode system in a 0.5 M Na_2SO_4 solution. (d) Band alignment of the BTEA-COF and EBA-COF.

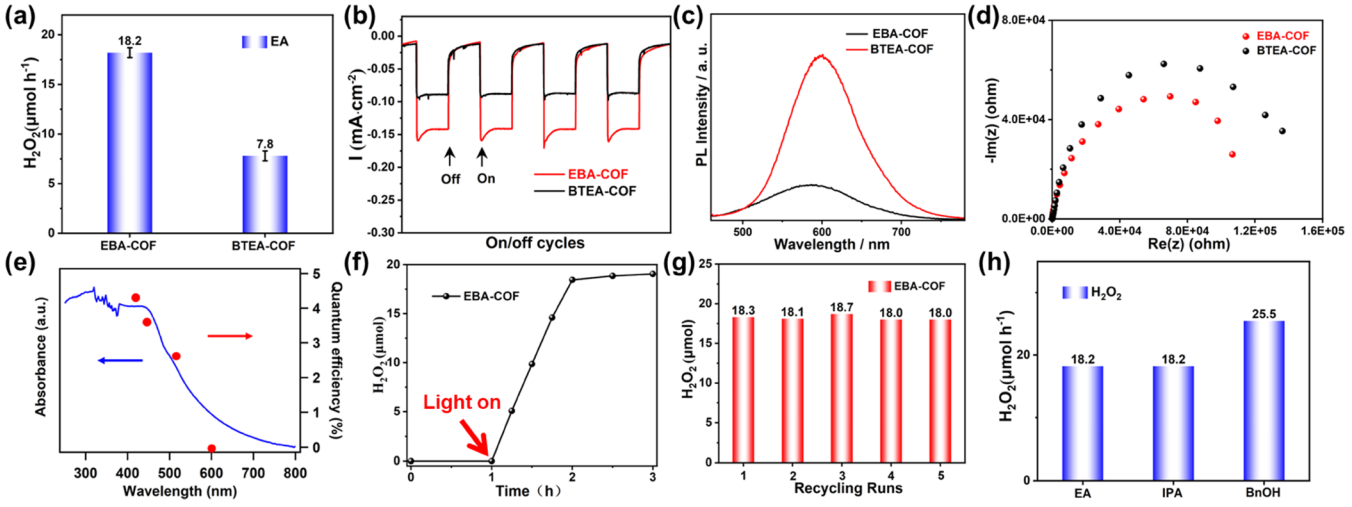

Figure 4. (a) H_2O_2 evolution rates. Reaction conditions: 10 mg of COF, 2.25 mL of H_2O, 0.25 mL of EA, 25 °C, and λ = 420 nm. (b) Transient photocurrents of the BTEA-COF and EBA-COF under visible light irradiation. (c) Photoluminescence emission spectra. (d) Electrochemical impedance spectra (EIS) of the BTEA-COF and EBA-COF photocatalysts under visible light irradiation. (e) Wavelength-dependent AQE of the EBA-COF photocatalyst. (f) Time course of H_2O_2 evolutions under visible light irradiation of the EBA-COF. (g) H_2O_2 production for five consecutive cycles using the EBA-COF. (h) EBA-COF for H_2O_2 production in different electron-donor sacrificial reagents.

positions matched well with the requirements for oxygen reduction to hydrogen peroxide (0.68 eV vs NHE), rendering these two COFs promising photocatalysts for H_2O_2 production.

Photocatalytic H_2O_2 production experiments were conducted under monochromatic light (420 nm LED). The H_2O_2 generation rates of the EBA-COF and BTEA-COF using ethanol (H_2O/EtOH = 9:1, v/v) as the sacrificial reagent were 1830 and 780 μmol h^{-1} g_{cat}^{-1}, respectively (Figure 4a,f). The enhanced H_2O_2 generation performance of the EBA-COF was presumably related to the lower CBM value compared to that of the BTEA-COF. The photocurrent of the EBA-COF was observed as ∼−0.16 mA cm^{-2}, which is twice higher than that of the BTEA-COF (∼−0.08 mA cm^{-2}), indicating faster photoresponse and more efficient separation of charge carriers in the EBA-COF (Figure 4b). Furthermore, the photoluminescence (PL) spectra of these two COFs were obtained to elucidate their charge recombination and separation characteristics. In a direct comparison of the PL intensities of the EBA-COF and BTEA-COF, it was evident that the EBA-COF exhibited a significantly lower PL intensity than that of the BTEA-COF (Figure 4c), indicating that charge separation was promoted and charge recombination was suppressed in the EBA-COF. In addition, the charge transfer rates for the EBA-COF and BTEA-COF were tested using electrochemical impedance spectroscopy (EIS). Accordingly, compared with the BTEA-COF, the EBA-COF showed a smaller radius of the semicircular Nyquist plot, indicating a higher interfacial charge transfer rate, which is beneficial for photocatalytic activity (Figure 4d). The significant difference in these semiconducting

https://doi.org/10.1021/acs.chemmater.2c00910
Chem. Mater. XXXX, XXX, XXX−XXX

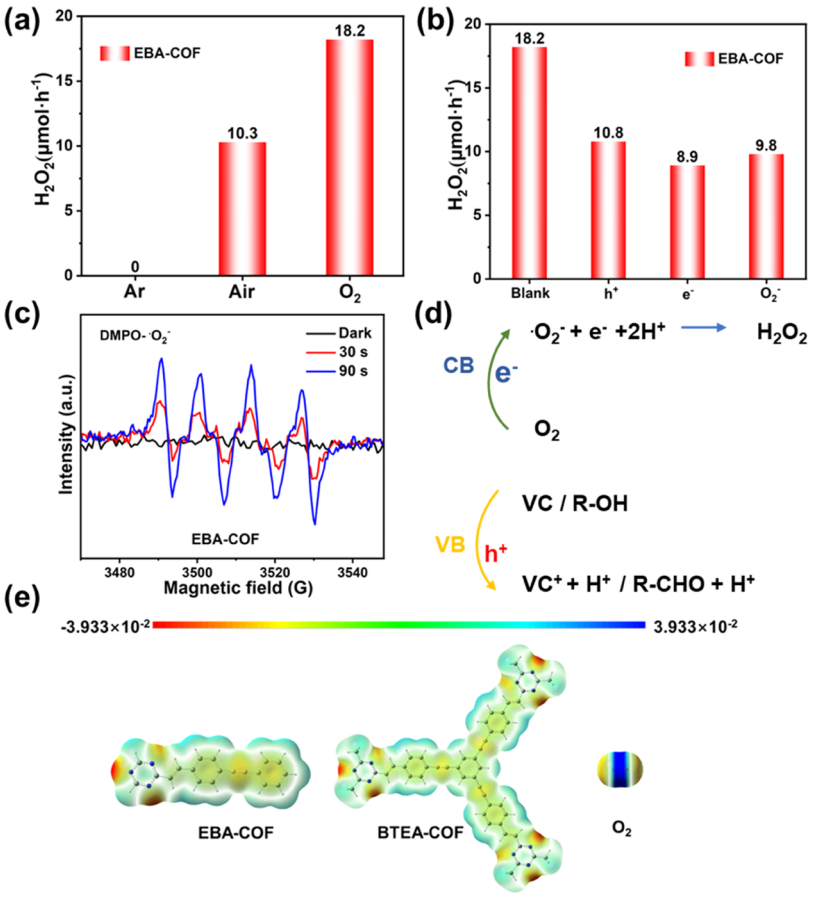

Figure 5. (a) Reactions under different gas atmospheres of EBA-COF. (b) Photocatalytic H_2O_2 production for the EBA-COF in KI, $CuSO_4$, and p-benzoquinone. (c) EPR trapping experiments in the presence of DMPO as an electron-trapping agent. (d) Proposed photocatalytic mechanism for the EBA-COF. (e) Optimized geometrical structures and the electrostatic potential surfaces for model systems of the EBA-COF, BTEA-COF, and O_2. All calculations were performed at the level of cam-B3LYP/6-31G(d)-GD3BJ. The red, green, and blue regions indicate negative, neutral, and positive electrostatic potentials, respectively.

properties between the two as-prepared COFs could arise from their intrinsic electronic structures. In addition, the contact angle on water of the EBA-COF and BTEA-COF was characterized (Figure S12). The result suggested that the contact angle of the EBA-COF is larger than that of the BTEA-COF, indicating that the better photocatalytic H_2O_2 production performance of the EBA-COF was attributed to the spatially structural characteristics. The EBA-COF outperformed the BTEA-COF in both photocurrent and EIS characteristics. Hence, the EBA-COF was expected to display a better photocatalytic activity. To quantify the spectral distribution of the photocatalytic activity of the EBA-COF, the apparent quantum efficiency (AQE) was measured as a function of the wavelength of the incident light using band-pass filters with central wavelengths of 420, 450, 520, and 600 nm (Figure 4e). The AQE of the EBA-COF was up to 4.4% at 420 nm. After photocatalytic H_2O_2 experiments, both COFs could retain their chemical structures (Figure S13) and morphology (Figure S14), whereas the PXRD patterns (Figure S15) disappeared and the peak of 001 facets became more obvious due to the exfoliation of both COFs during the photocatalytic H_2O_2 experiments.

For practical applications, the long-term photostability of catalysts is essential. The EBA-COF was used in five sequential 1 h photocatalytic H_2O_2 production runs (Figure 4g). There was no pronounced decline in the photoactivity over the last five cycles, suggesting the excellent stability of the EBA-COF. The H_2O_2 generation performance was further evaluated using various sacrificial reagents, including isopropanol (IPA) and benzyl alcohol (BnOH) (Figure 4h). The EBA-COF maintained the same H_2O_2 generation rate (1820 μmol h^{-1} g_{cat}^{-1}) using IPA as a sacrificial reagent. The highest H_2O_2 generation rate of the EBA-COF was achieved at 2550 μmol h^{-1} g_{cat}^{-1} in the presence of BnOH as a sacrificial reagent because the $\pi-\pi$ interaction between benzyl alcohol and the EBA-COF can effectively trap holes and promote the separation of electrons and holes. Notably, the H_2O_2 production rates of the EBA-COF and BTEA-COF are much higher than those of most of the previously reported COFs and comparable to those of other reported materials (Table S4). This was due to the enhanced charge transfer ability and suppressed charge recombination arising from spatially separated redox centers and the high crystallinity of the synthesized COFs.

To investigate the H_2O_2 production pathway during photocatalysis, we performed the test under different atmospheres. As illustrated in Figure 5a, the H_2O_2 production rate for the EBA-COF was highest under pure O_2, significantly lower than that under air, and nearly wholly inhibited under Ar. This strongly suggests that H_2O_2 was produced via oxygen reduction. In addition, as a control, electrons ($CuSO_4$), holes (KI), and $^{\bullet}O_2^-$ (p-benzoquinone) scavengers were added.

https://doi.org/10.1021/acs.chemmater.2c00910
Chem. Mater. XXXX, XXX, XXX−XXX

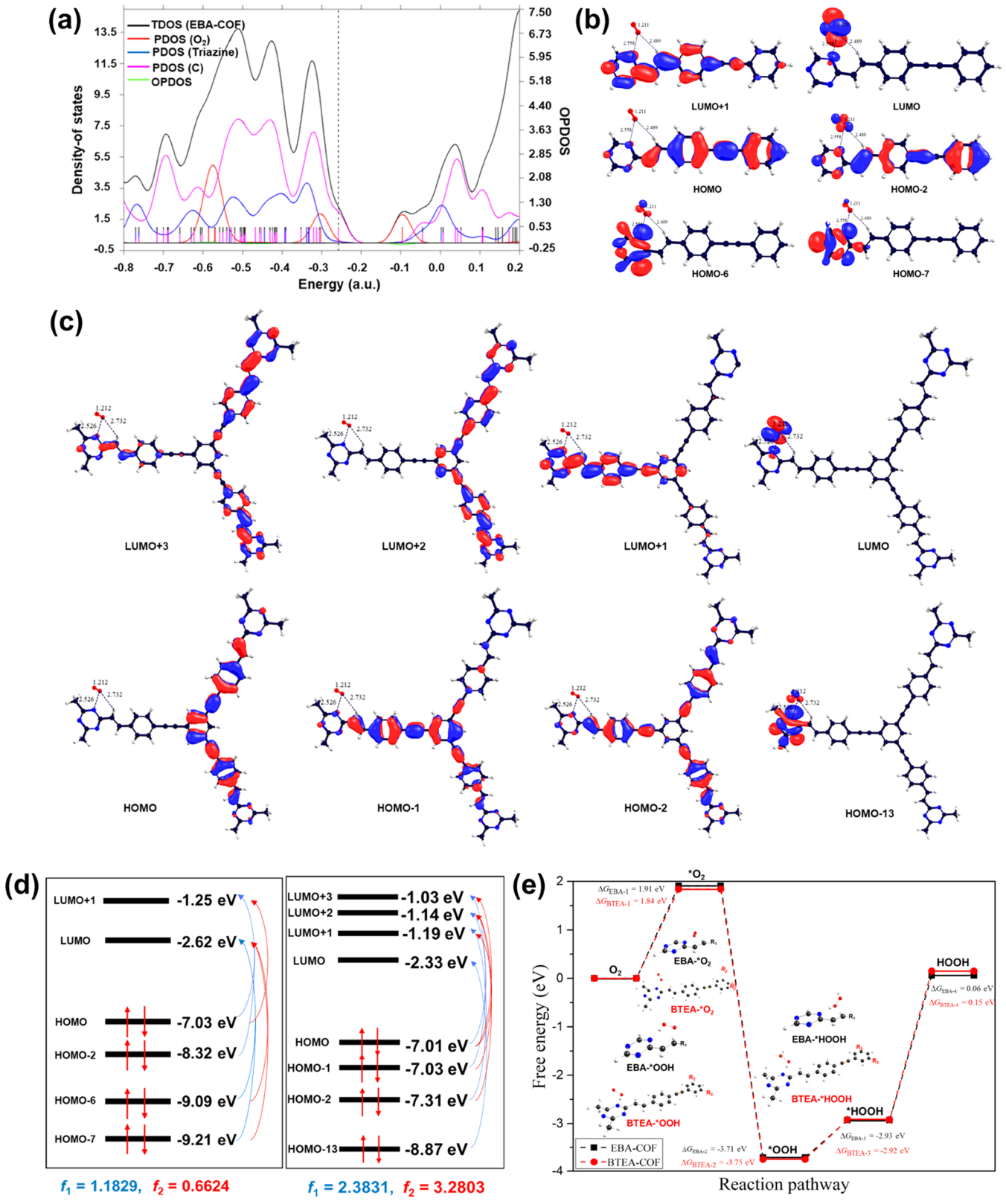

Figure 6. (a) Total density of states (TDOS) of the model system of the EBA-COF and the partial DOS of O_2, triazine, and carbon atoms. (b) Distributions of the highest occupied molecular orbital (HOMO) and the lowest unoccupied molecular orbital (LUMO), along with those of HOMO−2, HOMO−6, HOMO−7, and LUMO+1 for the model system of the EBA-COF. (c) Distributions of the highest occupied molecular orbital (HOMO) and the lowest unoccupied molecular orbital (LUMO), along with those of HOMO−2, HOMO−6, HOMO−7, and LUMO+1 for the model system of the BTEA-COF. (d) Calculated at the theoretical level of cam-B3LYP/6-31G(d)-GD3BJ (left: EBA-COF and right: BTEA-COF). (e) Calculated free energy diagrams of H_2O_2 production catalyzed by model systems of EBA-COF and BTEA-COF.

https://doi.org/10.1021/acs.chemmater.2c00910
Chem. Mater. XXXX, XXX, XXX−XXX

Notably, the H_2O_2 production performance of the EBA-COF was significantly decreased (Figure 5b), indicating that $^{\bullet}O_2^-$ was the active species during photocatalytic H_2O_2 generation. Electron paramagnetic resonance (EPR) measurements detected radicals using 5,5-dimethyl-1-pyrroline *N*-oxide (DMPO) as the trapping agent (Figure 5c). The typical signals of $^{\bullet}O_2^-$ were observed upon illumination, indicating the two-electron reduction of O_2. Based on these results, a proposed mechanism for photocatalytic H_2O_2 production by the EBA-COF was provided (Figure 5d).

To understand the catalytic mechanism of H_2O_2 production, we performed density functional theory (DFT) calculations with model systems of the EBA-COF and BTEA-COF. We optimized the geometrical structures of the two model systems without any restriction and calculated the electrostatic potential surfaces at the cam-B3LYP/6-31G(d)-GD3BJ theoretical level, as shown in Figure 5e. It could be deduced that acetylene and triazine units could be possible binding sites of triplet O_2. Based on the comparison of binding energies of the two sites and the smaller steric effect of the triazine unit, we find that the triazine unit could be the most possible catalytic site. The density of states (DOS) of the adsorption state of O_2 on the EBA-COF is shown in Figure 6a and that of the EBTA-COF is shown in Figure S16. In the vicinity of the highest occupied molecular orbital (HOMO) of the EBA-COF, basis functions from O_2 and triazine units contribute largely, which indicates that the triazine unit facilitates the catalytic process. To understand the photochemical process during the catalytic reaction, we further calculated the transition properties of the adsorption state with time-dependent DFT and list the calculated results in Figure 6b,c. Accordingly, for O_2 adsorption on the EBA-COF, the largest two oscillator strengths (f) are 1.1829 and 0.6624 (Figure 6d). The contribution mainly comes from the electron transition from the HOMO, HOMO−2, HOMO-6, and HOMO−7 to LUMO and LUMO+1. In the case of O_2 adsorption on the BTEA-COF, the contribution mainly stems from the transition from the HOMO, HOMO−1, HOMO−2, and HOMO−13 to LUMO, LUMO+1, LUMO+2, and LUMO+3. It should be emphasized that the orbitals including triazine unit contributions are largely (HOMO−6 and HOMO−7 in EBA-COF, and HOMO−13 in BTEA-COF) involved in the electron transition. Moreover, the electron transition gap is smaller for the EBA-COF than for the BTEA-COF. This suggests not only that the introduction of triazine is essential to the high efficiency of H_2O_2 production but also that the EBA-COF is more favorable than the BTEA-COF in the photocatalytic production of H_2O_2 from H_2O and O_2, although the thermodynamic characterizations are similar for the two COFs as shown in Figure 6e, which is consistent with experimental observations.

CONCLUSIONS

In summary, we developed two vinylene-linked COFs with spatially separated reaction centers using triazine- and acetylene-containing building units for photocatalytic H_2O_2 production. The photocatalytic production of H_2O_2 from H_2O and O_2 using this type of COF as a catalyst was then demonstrated for the first time. Our results suggest that the spatially separated and synergistic triazine and acetylene crosslinked by C═C bonds in these COFs could efficiently promote the charge separation and suppressed charge recombination, and these characteristics were beneficial for photocatalytic H_2O_2 production. The corresponding performance of both COFs was superior to that of many other reported organic catalysts and COFs over short reaction times. This work provides a new strategy for designing H_2O_2 production photocatalysts in the scaffolds of vinylene-linked COFs with synergistic photocatalytic active sites.

ASSOCIATED CONTENT

Supporting Information

The Supporting Information is available free of charge at https://pubs.acs.org/doi/10.1021/acs.chemmater.2c00910.

Preparation of COFs, details of the photocatalytic experiment, TGA curves, solid-state ^{13}C CP-MAS NMR spectrum, SEM and elemental mapping images, and comparison of photocatalytic H_2O_2 production properties (PDF)

AUTHOR INFORMATION

Corresponding Authors

Qing Xu − *CAS Key Laboratory of Low-Carbon Conversion Science and Engineering, Shanghai Advanced Research Institute (SARI), Chinese Academy of Sciences (CAS), Shanghai 201210, P. R. China;* orcid.org/0000-0002-9066-9837; Email: xuqing@sari.ac.cn

Xiong Chen − *State Key Laboratory of Photocatalysis on Energy and Environment, and Key Laboratory of Molecular Synthesis and Function Discovery, College of Chemistry, Fuzhou University, Fuzhou 350116, P. R. China;* orcid.org/0000-0003-2878-7522; Email: chenxiong987@fzu.edu.cn

Liwei Mi − *Henan Key Laboratory of Functional Salt Materials, Center for Advanced Materials Research, Zhongyuan University of Technology, Zhengzhou 450007, P. R. China;* orcid.org/0000-0001-9239-6599; Email: mlwzzu@163.com

Authors

Lipeng Zhai − *Henan Key Laboratory of Functional Salt Materials, Center for Advanced Materials Research, Zhongyuan University of Technology, Zhengzhou 450007, P. R. China;* orcid.org/0000-0002-0132-5611

Zhipeng Xie − *State Key Laboratory of Photocatalysis on Energy and Environment, and Key Laboratory of Molecular Synthesis and Function Discovery, College of Chemistry, Fuzhou University, Fuzhou 350116, P. R. China*

Cheng-Xing Cui − *School of Chemistry and Chemical Engineering, Henan Institute of Science and Technology, Xinxiang 453003, P. R. China*

Xiubei Yang − *Henan Key Laboratory of Functional Salt Materials, Center for Advanced Materials Research, Zhongyuan University of Technology, Zhengzhou 450007, P. R. China*

Xiating Ke − *State Key Laboratory of Photocatalysis on Energy and Environment, and Key Laboratory of Molecular Synthesis and Function Discovery, College of Chemistry, Fuzhou University, Fuzhou 350116, P. R. China*

Minghao Liu − *CAS Key Laboratory of Low-Carbon Conversion Science and Engineering, Shanghai Advanced Research Institute (SARI), Chinese Academy of Sciences (CAS), Shanghai 201210, P. R. China*

Ling-Bo Qu − *College of Chemistry, and Institute of Green Catalysis, Zhengzhou University, Zhengzhou 450001, P. R. China*

Complete contact information is available at: https://pubs.acs.org/10.1021/acs.chemmater.2c00910

Author Contributions

#L.Z., Z.X., and C.-X.C. contributed equally to this work. L.M., X.C., Q.X., and L.Z. designed this project. L.Z., Z.X., X.Y., X.K, and M.L. conducted the experiment. C.-X.C. conducted the theoretical calculation. L.M., X.C., Q.X., L.-B.Q., and L.Z. discussed the results and prepared the article.

Notes

The authors declare no competing financial interest.

■ ACKNOWLEDGMENTS

This work was supported by the National Natural Science Foundation of China (Grant No. U1804126, U1804129, 21671205, 21771164, 21972021, and 52103277) and the Support Program of Science and Technology Innovation Leading Talent of Zhongyuan (Grant No. 204200510014). L.Z. appreciates support from Key Projects of Science and Technology of Henan Province (Grant No. 212102210208) and the Zhongyuan University of Technology start-up grant. Q.X. acknowledges the financial support from the Natural Science Foundation of Shanghai (20ZR1464000).

■ REFERENCES

(1) Sato, K.; Aoki, M.; Noyori, R. A "green" route to adipic acid: direct oxidation of cyclohexenes with 30 percent hydrogen peroxide. *Science* **1998**, *281*, 1646−1647.

(2) Mase, K.; Yoneda, M.; Yamada, Y.; Fukuzumi, S. Seawater usable for production and consumption of hydrogen peroxide as a solar fuel. *Nat. Commun.* **2016**, *7*, No. 11470.

(3) Campos-Martin, J. M.; Blanco-Brieva, G.; Fierro, J. L. G. Hydrogen peroxide synthesis: an outlook beyond the anthraquinone process. *Angew. Chem., Int. Ed.* **2006**, *45*, 6962−6984.

(4) Zhang, P.; Tong, Y. W.; Liu, Y.; Vequizo, J. J. M.; Sun, H.; Yang, C.; Yamakata, A.; Fan, F.; Lin, W.; Wang, X.; Choi, W. Heteroatom dopants promote two-electron O_2 reduction for photocatalytic production of H_2O_2 on polymeric carbon nitride. *Angew. Chem., Int. Ed.* **2020**, *59*, 16209−16217.

(5) Shiraishi, Y.; Takii, T.; Hagi, T.; Mori, S.; Kofuji, Y.; Kitagawa, Y.; Tanaka, S.; Ichikawa, S.; Hirai, T. Resorcinol−formaldehyde resins as metal-free semiconductor photocatalysts for solar-to-hydrogen peroxide energy conversion. *Nat. Mater.* **2019**, *18*, 985−993.

(6) Chen, L.; Wang, L.; Wan, Y.; Zhang, Y.; Qi, Z.; Wu, X.; Xu, H. Acetylene and diacetylene functionalized covalent triazine frameworks as metal-free photocatalysts for hydrogen peroxide production: a new two-electron water oxidation pathway. *Adv. Mater.* **2020**, *32*, No. 1904433.

(7) Cai, J.; Huang, J.; Wang, S.; Iocozzia, J.; Sun, Z.; Sun, J.; Yang, Y.; Lai, Y.; Lin, Z. Crafting mussel-inspired metal nanoparticle-decorated ultrathin graphitic carbon nitride for the degradation of chemical pollutants and production of chemical resources. *Adv. Mater.* **2019**, *31*, No. 1806314.

(8) Gervasini, A.; Carniti, P.; Desmedt, F.; Miquel, P. Liquid phase direct synthesis of H_2O_2: activity and selectivity of Pd-dispersed phase on acidic niobia-silica supports. *ACS Catal.* **2017**, *7*, 4741−4752.

(9) Li, F.; Shao, Q.; Hu, M.; Chen, Y.; Huang, X. Hollow Pd-Sn nanocrystals for efficient direct H_2O_2 synthesis: the critical role of Sn on structure evolution and catalytic performance. *ACS Catal.* **2018**, *8*, 3418−3423.

(10) Freakley, S. J.; He, Q.; Harrhy, J. H.; Lu, L.; Crole, D. A.; Morgan, D. J.; Natainjua, E. N.; Edwards, J. K.; Carley, A. F.; Borisevich, A. Y.; Kiely, C. J.; Hutchings, G. J. Palladium-tin catalysts for the direct synthesis of H_2O_2 with high selectivity. *Science* **2016**, *351*, 965.

(11) Yang, S.; Verdaguer-Casadevall, A.; Arnarson, L.; Silvioli, L.; čolić, V.; Frydendal, R.; Rossmeisl, J.; Chorkendorff, I.; Stephens, E. L. Toward the decentralized electrochemical production of H_2O_2: a focus on the catalysis. *ACS Catal.* **2018**, *8*, 4064−4081.

(12) Ciriminna, R.; Albanese, L.; Meneguzzo, F.; Pagliaro, M. Hydrogen peroxide: a key chemical for today's sustainable development. *ChemSusChem* **2016**, *9*, 3374−3381.

(13) Li, L.; Xu, L.; Hu, Z.; Yu, J. Enhanced mass transfer of oxygen through a gas−liquid−solid interface for photocatalytic hydrogen peroxide production. *Adv. Funct. Mater.* **2021**, *31*, No. 2106120.

(14) He, C.; Liang, J.; Zou, Y.-H.; Yi, J.-D.; Huang, Y.-B.; Cao, R. Metal-organic frameworks bonded with metal N-heterocyclic carbenes for efficient catalysis. *Natl. Sci. Rev.* **2021**, No. nwab157.

(15) He, C.; Wu, Q.-J.; Mao, M.-J.; Zou, Y.-Z.; Liu, B.-T.; Huang, Y.-B.; Cao, R. Multifunctional gold nanoparticles@imidazolium-based cationic covalent triazine frameworks for efficient tandem reactions. *CCS Chem.* **2020**, *2*, 2368−2380.

(16) Meng, D.-L.; Zhang, M.-D.; Si, D.-H.; Mao, M.-J.; Hou, Y.; Huang, Y.-B.; Cao, R. Highly selective tandem electroreduction of CO_2 to ethylene over atomically isolated nickel-nitrogen site/copper nanoparticle catalysts. *Angew. Chem., Int. Ed.* **2021**, *60*, 25485−25492.

(17) Shiraishi, Y.; Kanazawa, S.; Kofuji, Y.; Sakamoto, H.; Ichikawa, S.; et al.*et al.* Sunlight-driven hydrogen peroxide production from water and molecular oxygen by metal-free photocatalysts. *Angew. Chem., Int. Ed.* **2014**, *53*, 13454−13459.

(18) Hou, H.; Zeng, X.; Zhang, X. Production of hydrogen peroxide by photocatalytic processes. *Angew. Chem., Int. Ed.* **2020**, *59*, 17356−17376.

(19) Sun, Y.; Han, L.; Strasser, P. A comparative perspective of electrochemical and photochemical approaches for catalytic H_2O_2 production. *Chem. Soc. Rev.* **2020**, *49*, 6605−6631.

(20) Teng, Z.; Zhang, Q.; Yang, H.; Kato, K.; Yang, W.; Lu, Y.-R.; Liu, S.; Wang, C.; Yamakata, A.; Su, C.; Liu, B.; Ohno, T. Atomically dispersed antimony on carbon nitride for the artificial photosynthesis of hydrogen peroxide. *Nat. Catal.* **2021**, *4*, 374−384.

(21) Wei, Z.; Liu, M.; Zhang, Z.; Yao, W.; Tan, H.; Zhu, Y. Efficient visible-light-driven selective oxygen reduction to hydrogen peroxide by oxygen-enriched graphitic carbon nitride polymers. *Energy Environ. Sci.* **2018**, *11*, 2581−2589.

(22) He, Z.; Kim, C.; Lin, L.; Jeon, T. H.; Lin, S.; Wang, X.; Choi, W. Formation of heterostructures via direct growth CN on h-BN porous nanosheets for metal-free photocatalysis. *Nano Energy* **2017**, *42*, 58−68.

(23) Zheng, Y.; Yu, Z.; Ou, H.; Asiri, A. M.; Chen, Y.; Wang, X. Black phosphorus and polymeric carbon nitride heterostructure for photoinduced molecular oxygen activation. *Adv. Funct. Mater.* **2018**, *28*, No. 1705407.

(24) Shiraishi, Y.; Matsumoto, M.; Ichikawa, S.; Tanaka, S.; Hirai, T. Polythiophene-doped resorcinol-formaldehyde resin photocatalysts for solar-to-hydrogen peroxide energy conversion. *J. Am. Chem. Soc.* **2021**, *143*, 12590−12599.

(25) Shiraishi, Y.; Takii, T.; Hagi, T.; Mori, S.; Kofuji, Y.; Kitagawa, Y.; Tanka, S.; Ichikawa, S.; Hirai, T. Resorcinol−formaldehyde resins as metal-free semiconductor photocatalysts for solar-to-hydrogen peroxide energy conversion. *Nat. Mater.* **2019**, *18*, 985−993.

(26) Liu, L.; Gao, M.-Y.; Yang, H. F.; Wang, X.; Li, X.; Cooper, A. I. Linear conjugated polymers for solar-driven hydrogen peroxide production: the importance of catalyst stability. *J. Am. Chem. Soc.* **2021**, *143*, 19287−19293.

(27) Chen, L.; Wang, L.; Wan, Y.; Zhang, Y.; Qi, Z.; Wu, X.; Xu, H. Acetylene and diacetylene functionalized covalent triazine frameworks as metal-free photocatalysts for hydrogen peroxide production: a new two-electron water oxidation pathway. *Adv. Mater.* **2020**, *32*, No. 1904433.

(28) Che, H.; Gao, X.; Chen, J.; Hou, J.; Ao, Y.; Wang, P. Iodide-induced fragmentation of polymerized hydrophilic carbon nitride for

high-performance quasi-homogeneous photocatalytic H_2O_2 production. *Angew. Chem., Int. Ed.* **2021**, *60*, 25546−25550.
(29) Chen, W.; Wang, L.; Mo, D.; He, F.; Wen, Z.; Wu, X.; Xu, H.; Chen, L. Modulating benzothiadiazole-based covalent organic frameworks via halogenation for enhanced photocatalytic water splitting. *Angew. Chem., Int. Ed.* **2020**, *59*, 16902−16909.
(30) Chen, D.; Chen, W.; Zhang, G.; Li, S.; Chen, W.; Xing, G.; Chen, L. N-Rich 2D heptazine covalent organic frameworks as efficient metal-free photocatalysts. *ACS Catal.* **2022**, *12*, 616−623.
(31) Jin, E.; Lan, Z.; Jiang, Q.; Geng, K.; Li, G.; Wang, X.; Jiang, D. 2D sp^2 carbon-conjugated covalent organic frameworks for photocatalytic hydrogen production from water. *Chem* **2019**, *5*, 1632−1647.
(32) Wang, Y.; Hao, W.; Liu, H.; Chen, R.; Pan, Q.; Li, Z.; Zhao, Y. Facile construction of fully sp^2-carbon conjugated two-dimensional covalent organic frameworks containing benzobisthiazole units. *Nat. Commun.* **2022**, *13*, No. 100.
(33) Gottschling, K.; Savasci, G.; Vignolo-González, H.; Schmidt, S.; Mauker, P.; Banerjee, T.; Rovó, P.; Ochsenfeld, C.; Lotsch, B. V. Rational design of covalent cobaloxime−covalent organic framework hybrids for enhanced photocatalytic hydrogen evolution. *J. Am. Chem. Soc.* **2020**, *142*, 12146−12156.
(34) Wang, X.; Chen, L.; Chong, S. Y.; Little, M. A.; Wu, Y.; Zhu, W.-H.; Clowes, R.; Yan, Y.; Zwijnenburg, M. A.; Sprick, R. S.; Cooper, A. I. Sulfone-containing covalent organic frameworks for photocatalytic hydrogen evolution from water. *Nat. Chem.* **2018**, *10*, 1180−1189.
(35) Li, W.; Huang, X.; Zeng, T.; Liu, Y. A.; Hu, W.; Yang, H.; Zhang, Y.-B.; Wen, K. Thiazolo[5,4-d]thiazole-based donor-acceptor covalent organic framework for sunlight-driven hydrogen evolution. *Angew. Chem., Int. Ed.* **2021**, *60*, 1869−1874.
(36) Mi, Z.; Zhou, T.; Weng, W.; Unruangsri, J.; Hu, K.; Yang, W.; Wang, C.; Zhang, K. A. I.; Guo, J. Covalent organic frameworks enabling site isolation of viologen-derived electron-transfer mediators for stable photocatalytic hydrogen evolution. *Angew. Chem., Int. Ed.* **2021**, *60*, 9642−9649.
(37) Zhang, S.; Cheng, G.; Guo, L.; Wang, N.; Tan, B.; Jin, S. Strong-base-assisted synthesis of a crystalline covalent triazine framework with high hydrophilicity via benzylamine monomer for photocatalytic water splitting. *Angew. Chem., Int. Ed.* **2020**, *59*, 6007−6014.
(38) Chen, R.; Wang, Y.; Ma, Y.; Mal, A.; Gao, X.-Y.; Gao, L.; Qiao, L.; Li, X.-B.; Wu, L.-Z.; Wang, C. Rational design of isostructural 2D porphyrin-based covalent organic frameworks for tunable photocatalytic hydrogen evolution. *Nat. Commun.* **2021**, *12*, No. 1354.
(39) Wu, Q.; Xie, R.-K.; Mao, M.-J.; Chai, G.-L.; Yi, J.-D.; Zhao, S.-S.; Huang, Y.-B.; Cao, R. Integration of strong electron transporter tetrathiafulvalene into metalloporphyrin-based covalent organic framework for highly efficient electroreduction of CO_2. *ACS Energy Lett.* **2020**, *5*, 1005−1012.
(40) Krishnaraj, C.; Jena, H. S.; Bourda, L.; Laemont, A.; Pachfule, P.; Roeser, J.; Chandran, C. V.; Borgmans, S.; Rogge, S. M. J.; Leus, K.; Stevens, C. V.; Martens, J. A.; Speybroeck, V. V.; Breynaert, E.; Thomas, A.; Voort, P. V. D. Strongly reducing (diarylamino)benzene-based covalent organic framework for metal-free visible light photocatalytic H_2O_2 generation. *J. Am. Chem. Soc.* **2020**, *142*, 20107−20116.
(41) Li, L.; Xu, L.; Hu, Z.; Yu, J. C. Enhanced mass transfer of oxygen through a gas−liquid-solid interface for photocatalytic hydrogen peroxide production. *Adv. Funct. Mater.* **2021**, *31*, No. 2106120.
(42) Kou, M.; Wang, Y.; Xu, Y.; Ye, L.; Huang, Y.; Jia, B.; Li, H.; Ren, J.; Deng, Y.; Chen, J.; Zhou, Y.; Lei, K.; Wang, L.; Liu, W.; Huang, H.; Ma, T. Molecularly Engineered Covalent Organic Frameworks for Hydrogen Peroxide Photosynthesis. *Angew. Chem., Int. Ed.* **2022**, *61*, No. e202200413.
(43) Lyu, H.; Diercks, C. S.; Zhu, C.; Yaghi, O. M. Porous crystalline olefin-linked Covalent organic frameworks. *J. Am. Chem. Soc.* **2019**, *141*, 6848−6852.
(44) Bi, S.; Thiruvengadam, P.; Wei, S.; Zhang, W.; Zhang, F.; Gao, L.; Xu, J.; Wu, D.; Chen, J.-S.; Zhang, F. Vinylene-bridged two-dimensional covalent organic frameworks via Knoevenagel condensation of tricyanomesitylene. *J. Am. Chem. Soc.* **2020**, *142*, 11893−11900.
(45) Xu, J.; He, Y.; Bi, S.; Wang, M.; Yang, P.; Wu, D.; Wang, J.; Zhang, F. An olefin-linked covalent organic framework as a flexible thin-film electrode for a high-performance micro-supercapacitor. *Angew. Chem.* **2019**, *131*, 12193−12197.
(46) Wei, S.; Zhang, F.; Zhang, W.; Qiang, P.; Yu, K.; Fu, X.; Wu, D.; Bi, S.; Zhang, F. Semiconducting 2D triazine-cored covalent organic frameworks with unsubstituted olefin linkages. *J. Am. Chem. Soc.* **2019**, *141*, 14272−14279.
(47) Bi, S.; Yang, C.; Zhang, W.; Xu, J.; Liu, L.; Wu, D.; Wang, X.; Han, Y.; Liang, Q.; Zhang, F. Two-dimensional semiconducting covalent organic frameworks via condensation at arylmethyl carbon atoms. *Nat. Commun* **2019**, *10*, No. 2467.
(48) Cui, W.-R.; Zhang, C.-R.; Jiang, W.; Li, F-F.; Liang, R.-P.; Liu, J.; Qiu, J.-D. Regenerable and stable sp^2 carbon-conjugated covalent organic frameworks for selective detection and extraction of uranium. *Nat. Commun* **2020**, *11*, No. 436.
(49) Jin, E.; Asada, M.; Xu, Q.; Dalapati, S.; Addicoat, M. A.; Brady, M. A.; Xu, H.; Nakamura, T.; Heine, T.; Chen, Q.; Jiang, D. Two-dimensional sp^2 carbon-conjugated covalent organic frameworks. *Science* **2017**, *357*, 673−676.
(50) Jin, E.; Gen, K.; Lee, K. H.; Jiang, W.; Li, J.; Jiang, Q.; Irle, S.; Jiang, D. Topology-templated synthesis of crystalline porous covalent organic frameworks. *Angew. Chem., Int. Ed.* **2020**, *59*, 12162−12169.
(51) Chen, R.; Shi, J.; Ma, Y.; Lin, G.; Lang, X.; Wang, C. Designed synthesis of a 2D porphyrin-based sp^2 carbon-conjugated covalent organic framework for heterogeneous photocatalysis. *Angew. Chem., Int. Ed.* **2019**, *58*, 6430−6434.
(52) Wang, Z.; Yang, Y.; Zhao, Z.; Zhang, P.; Zhang, Y.; Liu, J.; Ma, S.; Cheng, P.; Chen, Y.; Zhang, Z. Green synthesis of olefin-linked covalent organic frameworks for hydrogen fuel cell applications. *Nat Commun.* **2021**, *12*, No. 1982.
(53) Zhang, F.; Wei, S.; Wei, W.; Zou, J.; Gu, G.; Wu, D.; Bi, S.; Zhang, F. Trimethyltriazine-derived olefin-linked covalent organic framework with ultralong nanofibers. *Sci. Bull.* **2020**, *65*, 1659−1666.
(54) Cheng, H.; Lv, H.; Cheng, J.; Wang, L.; Wu, X.; Xu, H. Rational design of covalent heptazine frameworks with spatially separated redox centers for high-efficiency photocatalytic hydrogen peroxide production. *Adv. Mater.* **2021**, *34*, No. 2107480.

https://doi.org/10.1021/acs.chemmater.2c00910
Chem. Mater. XXXX, XXX, XXX−XXX